10-7-2023

Increased ductility of Ti-6Al-4V by interlayer milling during directed energy deposition

Rakeshkumar Karunakaran

Luz D. Sotelo

Hitarth Maharaja

Calsey Nez

Monsuru Ramoni

See next page for additional authors

Authors

Rakeshkumar Karunakaran, Luz D. Sotelo, Hitarth Maharaja, Calsey Nez, Monsuru Ramoni, Scott Halliday, Sushil Mishra, Joseph A. Turner, and Michael P. Sealy

Increased ductility of Ti-6Al-4V by interlayer milling during directed energy deposition

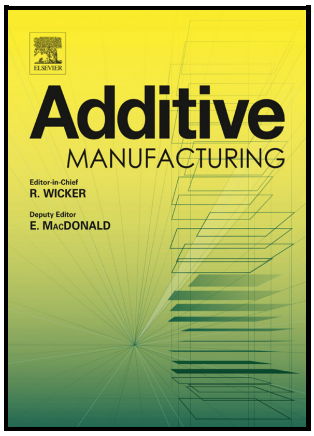

Rakeshkumar Karunakaran, Luz D. Sotelo, Hitarth Maharaja, Calsey Nez, Monsuru Ramoni, Scott Halliday, Sushil Mishra, K.P. Karunakaran, Joseph A. Turner, Michael P. Sealy

PII: S2214-8604(23)00431-1

DOI: https://doi.org/10.1016/j.addma.2023.103818

Reference: ADDMA103818

To appear in: *Additive Manufacturing*

Received date: 27 April 2023
Revised date: 4 October 2023
Accepted date: 7 October 2023

Please cite this article as: Rakeshkumar Karunakaran, Luz D. Sotelo, Hitarth Maharaja, Calsey Nez, Monsuru Ramoni, Scott Halliday, Sushil Mishra, K.P. Karunakaran, Joseph A. Turner and Michael P. Sealy, Increased ductility of Ti-6Al-4V by interlayer milling during directed energy deposition, *Additive Manufacturing,* (2023) doi:https://doi.org/10.1016/j.addma.2023.103818

Increased ductility of Ti-6Al-4V by interlayer milling during directed energy deposition

Rakeshkumar Karunakaran[a], Luz D. Sotelo[a], Hitarth Maharaja[b], Calsey Nez[c], Monsuru Ramoni[c], Scott Halliday[c], Sushil Mishra[b], K. P. Karunakaran[b], Joseph A. Turner [d], Michael P. Sealy*[a,d]

[a] *School of Mechanical Engineering, Purdue University, West Lafayette, IN 47907, U.S.A.*

[b] *Department of Mechanical Engineering, Indian Institute of Technology Bombay, Mumbai, 400076, India*

[c] *Industrial Engineering, School of Engineering, Math and Technology, Navajo Technical University, Crownpoint, NM 87313, U.S.A.*

[d] *Department of Mechanical and Materials Engineering, University of Nebraska-Lincoln, Lincoln, NE 68588, U.S.A.*

Abstract

Additive manufacturing (AM) often results in high strength but poor ductility in titanium alloys. Hybrid AM is a solution capable of improving both ductility and strength. In this study, hybrid AM of Ti-6Al-4V was achieved by coupling directed energy deposition with interlayer machining. The microstructure, residual stress, and microhardness were examined to explain how interlayer machining caused a 63% improvement in ductility while retaining an equivalent strength to as-printed samples. Interlayer machining introduced recurrent interruptions in printing that allowed for slow cooling-induced coarsening of acicular α laths at the machined interfaces. The coarse α laths on the selectively machined layers increased dislocation motion under tensile loads and improved bulk ductility. The results highlighted in this publication demonstrate the feasibility of hybrid AM to enhance the toughness of titanium alloys.

Keywords:
hybrid additive manufacturing, milling, directed energy deposition, titanium

1. Introduction

1.1 Challenges in Hybrid Additive-Subtractive Manufacturing

Conventional fabrication of titanium alloys uses cutting tools that are expensive and time-consuming due to poor machinability [1]. Conventionally machined titanium surfaces also have a high affinity for oxidation, necessitating atmospheric control during fabrication. Rather than bulk machining wrought titanium, an alternative is to couple machining with 3D printing of near-net shape components. Improved material utilization by AM reduces the machining requirements, and the total manufacturing time shortens by eliminating tooling and fixtures for work holding. AM technologies like directed energy deposition (DED) are popular for fabricating titanium due to their high manufacturing speed and low powder usage [3]. However, DED-printed parts are less precise than powder bed fusion. This disadvantage is often overcome by coupling DED with subtractive post-processes like milling or grinding to remove excess material from near-net depositions. Interlayer milling is also a means to remove imperfectly deposited layers during printing, which improves the productivity of AM systems [2].

A critical technical barrier in additively manufactured Ti-6Al-4V titanium alloy, even after subtractive post-processing, is low ductility and high anisotropy [4]. Hot isostatic pressing and annealing are popular approaches to mitigate anisotropy and improve ductility, but strength is reduced [5]. Additionally, these approaches are ineffective post-production solutions for managing *in situ* distortion and tensile residual stress buildup during DED. One solution to improve the mechanical behavior (strength *and* ductility) of titanium fabricated by DED is hybrid AM with interlayer mechanical treatments. Coupling AM with interlayer milling effectively alters mechanical properties and achieves the required part tolerances. Hybrid AM [6] with secondary processes alongside printing, like laser shock peening, improve mechanical behavior through microstructural gradients and compressive residual stress [7, 8].

1.2 Research Objectives

While laser shock peening improves performance through high strain rate (> 10^5/s) coldworking, dry machining is a low strain rate thermo-mechanical process that introduces a local thermal gradient from tool-workpiece interactions and likely some amount of hot burnishing from material flow under the neutral point of the cutting tool. The effects of low strain rate (< 10^3/s) interlayer milling in hybrid AM are largely unexplained. In this research, DED was coupled with interlayer milling to identify the underlying mechanisms governing mechanical behavior of Ti-6Al-4V fabricated by hybrid AM.

Since interlayer machining is pertinent to achieve uniform layers by avoiding overbuilding, the authors addressed a key scientific question on how such intermittent machining steps alter local material characteristics. Specifically, the objective was to determine if the thermal history from localized, recurrent annealing from the heat flux thermally cancels compressive residual stress and grain refinement imparted by interlayer milling. That is, does the heat remove beneficial mechanical properties imparted by milling? This objective is rooted in two primary hypotheses. First, the effects of low strain rate deformation (< 10^3/s) by milling are retained during subsequent printing such that friction from dry milling generates localized heat flux and plastic deformation in the workpiece that refines and dynamically recrystallizes hybrid layers to nucleate stress-free grains. Second, the inherent and recurrent dwell time introduced by interlayer machining during printing results in a spatially graded grain size distribution within the titanium deposition, where the selectively machined interfaces with coarse α laths improves bulk ductility. The approach was to characterize microstructure, microhardness, residual stress, and tensile strength. This study forms the groundwork for understanding material behavior from hybrid DED systems.

1.3 Microstructure Formation from Additive-Subtractive Manufacturing of Ti-6Al-4V

1.3.1 Microstructure of Ti-6Al-4V

Ti-6Al-4V is an allotropic alloy that exists as body centered cubic (BCC) β grains above the β-transus temperature (980 °C) [9]. Ti-6Al-4V cooled below β-transus temperature undergoes phase transformation to hexagonal close packed (HCP) α grains. The β grains in rapid cooled (faster than 410 °C/s) regions of printed Ti-6Al-4V decompose by diffusionless phase transformation into acicular martensitic grains (α') by non-equilibrium transformation [9]. The β grains in slow-cooled regions (slower than 410 °C/s) undergo equilibrium diffusion transformation into α + β grains.

1.3.2 Microstructure from DED

The melting and reheating of Ti-6Al-4V layers by DED evolve complicated columnar microstructures. The laser beam used in DED creates a moving heat flux that melts the deposited powder and reheats underlying deposited layers. The molten layers, after deposition, cool by forced convection from the assist gas and heat conduction into the substrate. The repetitive heating cycles from subsequent layer depositions influence microstructural orientation and composition that affect mechanical behavior [10]. The orientation of columnar prior β grains corresponds to laser raster pattern and build direction [11], and causes anisotropy in printed Ti-6Al-4V [12]. In addition to influencing microstructure formation, raster patterns influence heat accumulation during printing, leading to over-melting and cracking [13].

1.3.3 Microstructure from Machining

The repetitive heat treatment cycles from printing forms complex solidified microstructure that responds uniquely to machining forces in comparison to microstructure from conventional processing [14]. Specifically for printed titanium, low thermal conductivity (7-38 W/mK [15]) presents an added challenge by preventing heat dissipation away from the cutting tool during machining. The high heat gradient within the heat affected zone gives rise to thermal softening in titanium when machining temperatures exceed 800 °C [16]. Thermal softening tends to dominate over strain hardening and dynamic recovery in high temperature and strain rate conditions to lower the local flow stress near milled surfaces [17, 18]. In this work, local alterations to

stress-strain relationships from interlayer milling were expected to cause a bulk reduction in the flow stress, strength, and hardness while increasing ductility of printed titanium.

1.3.4 Microstructure Formation Mechanisms in Hybrid AM

Interlayer mechanical surface treatments improve surface and bulk (*i.e.*, glocal [6]) integrity by redistributing residual stress and grain refinement. The plausible mechanisms governing the material behavior when DED is coupled with interlayer machining are provided in Fig. 1. DED generates large spatial thermal gradients in titanium that form hard and brittle α laths [9]. Dwell time introduced during printing softens the fine microstructure by grain coarsening due to prolonged holding at high temperatures. The microstructure formed by DED was expected to be influenced by machining-induced work-hardening or dynamic recrystallization. Work-hardening forms a hard and brittle machined subsurface, whereas dynamic recrystallization yields a soft and ductile subsurface. If the working temperature is below 700 °C, work-hardening is the leading mechanism in interlayer machining to dictate microstructure in the Widmanstätten matrix [16]. This is because dislocations accumulated from deformation increase dislocation density within grains and prevent further deformation, which translates to low ductility and increased hardness. Alternatively, high strain rate deformation coupled with a local increase in temperature may cause dynamic recrystallization at machined interfaces, which will nucleate unstressed fine grains that are soft and ductile.

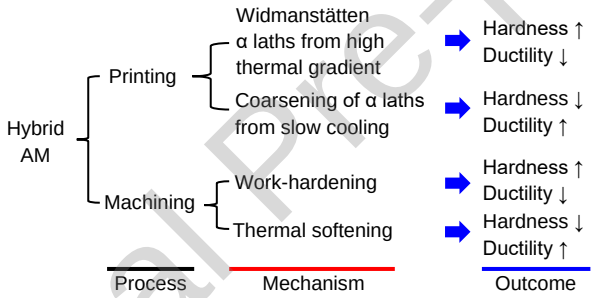

Fig. 1 Microstructural mechanisms guiding material behavior in hybrid additive-subtractive manufacturing of titanium [19, 20].

1.4 Residual Stress from Hybrid AM

Large thermal gradients in DED cause tensile residual stress in upper layers that distort deposited layers and initiate cracking if the yield strength is exceeded [21, 22]. DED tool path planning strategies mitigate distortion by controlling heat gradients within layers but are unable to prevent tensile stress accumulation in upper portions of builds [29, 30]. Hybrid AM coupling printing with secondary surface treatments provides a better pathway for residual stress management. Hybrid AM with laser shock peening as the surface treatment on 420 stainless steel induced compressive stress up to a measurable depth of 2 mm from the top surface [23]. Another hybrid AM technique coupled DED with ultrasonic peening on every layer to show a 115 MPa reduction in tensile residual stress in a Ni-based alloy [24]. While the two peening techniques improve failure strain by imparting compressive stress and work hardening, dry milling titanium creates a thermo-mechanical environment with local heat gradients and compressive residual stress (~250 MPa [25]). Strengthening mechanisms for such adiabatically sheared titanium surfaces subjected to repeated thermal gradients are not well established and are explored in this research. Unstressed α laths nucleated from dynamic recrystallization on milled interfaces may disturb fine α+β microstructure from DED and alter stress fields that affect failure strain. The grain growth and residual stress is also affected by the inherent dwell time in printing introduced by interlayer machining that increases distortion [26]. Therefore, the thermo-mechanical phenomena of

interlayer milling is important in accurately predicting the performance of hybrid AM fabricated titanium components in service environments.

1.5 Enhanced Mechanical Behavior from Hybrid AM

For additively manufactured Ti-6Al-4V, thermal gradients during DED evolve columnar prior β grains containing fine Widmanstätten (*i.e.*, basket-weave) α [10] or martensitic α' [11] grains that anisotropically change bulk strength and ductility [27]. The part strength is particularly low (800 MPa ultimate tensile strength) along the build direction due to porosity and lack of fusion at layer interfaces compared to wrought (1050 MPa ultimate tensile strength) [4]. Within the part, the highest strength resides within the core or interior of builds due to smaller thermal gradients from conduction and reheating that limit internal crack formation. In terms of plastic strain, hybrid AM coupling DED and laser shock peening demonstrated a 50 % improvement under quasistatic compression by cold working and grain refinement with no change in strength [28]. Other AM processes like powder bed fusion coupled with interlayer mechanical treatments like ultrasonic peening also demonstrated similar improvements to material performance [29]. In the case of thermo-mechanical loading from milling, it is important to understand if and how interlayer changes influence bulk mechanical behavior.

2. Materials and Methods

2.1 Ti-6Al-4V Powder Characterization

The Ti-6Al-4V titanium alloy powder used in this study was spherical and had satellite particles (Fig. 2). Five images of fresh powder were captured using a scanning electron microscope at 150X magnification for quantifying powder size distribution. A total of 123 powder particles were analyzed from these images by ImageJ to determine D_{10}, D_{50}, and D_{90} of 72 µm, 88 µm, and 105 µm, respectively. The average particle size was 93 µm.

Excess powder sprayed from deposition nozzles was collected and sieved in inert atmosphere to prevent oxidation. Re-use of sieved powder was limited to three times to minimize the influence of powder oxidation. Printing tasks were completed within five months of receiving fresh powder as an added measure against oxidation. Thermogravimetry analysis (TGA) was performed on fresh and reused Ti-6Al-4V powder as a quality control measure for moisture formation. Moisture absorbed by reused powder was quantified using TGA 209 F1 Libra, wherein 50 mg of Ti-6Al-4V powder was placed in a crucible and heated to 200 °C under a nitrogen atmosphere. Any moisture present in the sample evaporated and weight loss was measured. No significant difference in moisture gain was observed (0.10 % decrease in mass at 200 °C) in Ti-6Al-4V powder due to re-use.

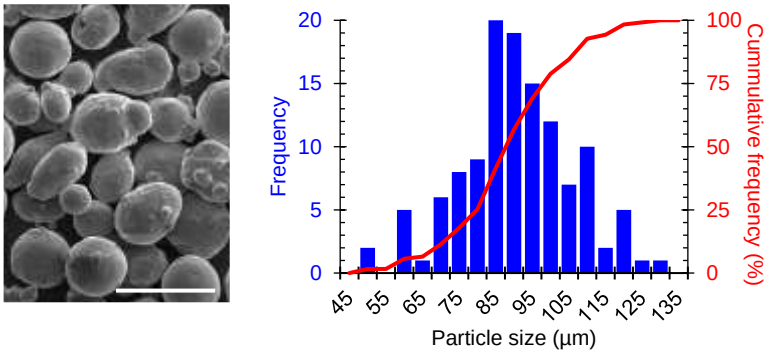

Fig. 2 Ti-6Al-4V powder (a) morphology and (b) particle size distribution.

2.2 Hybrid AM by DED and Milling

This investigation used the Optomec LENS 500 Controlled Atmosphere System, commercially referred to as laser engineering net shaping (LENS™), to deliver material using four nozzles and melted powder using a fiber laser (Fig. 3). The system maintained a sealed argon environment to keep oxygen under 40 ppm. The argon assist gas flow from center purge and powder nozzles was 30 L/min and 6 L/min, respectively. All printing was performed on 25 mm thick Ti-6Al-4V baseplates. Other significant DED process parameters for the builds are indicated in Table 1. The DED parameters were selected from a prior study that focused on characterizing ultrasound backscatter signal from microstructure of printed Ti-6Al-4V [30]. The ultrasound characterization technique was applied in this research, as described in sections 2.3.2 and 3.2. The samples were printed with a bidirectional 0°/90° raster pattern, *i.e.*, the deposition raster in each layer was rotated 90° to the previous layer. The density of samples printed for this research was above 98% as per Archimedes' method.

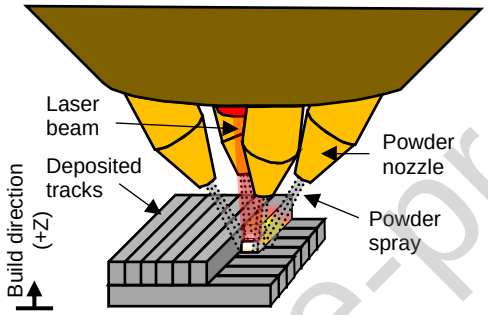

Fig. 3 Schematic of DED using LENS.

Table 1 Process parameters for DED

Parameter	Value
Laser spot diameter:	600 µm
Laser power:	500 W
Laser scanning speed:	1 m/min
Powder flow rate:	3 g/min
Layer thickness:	460 µm
Hatch spacing:	300 µm

In situ (*i.e.*, in-place) stress management by milling during DED necessitates dry cutting to avoid contamination of expensive Ti-6Al-4V powder. Milling was conducted *in situ* by a 19.1 mm diameter tetra end mill cutter (Ingersoll INGCUT 2910942 1TJ1C-07030S7R01) with carbide inserts (Ingersoll INGCUT 6167059 ENHU050308R-PH). This cutting insert is meant for high temperature cutting and titanium alloys and contained a TiCN/Al2O3/TiN coating (Grade IN7035). The corner radius was 0.79 mm, and the cutting edge length was 4.6 mm. Schematic of the hybrid AM system is shown in Fig. 4. Machining parameters are provided in Table 2. All hybrid samples except those for residual stress analysis were interlayer milled by a single pass of the milling cutter over the sample surfaces. The width of residual stress analysis samples was broader than the cutter diameter to accommodate strain gauges. Therefore, two passes of face milling were performed with a 14 mm radial depth of cut.

Table 2 Process parameters for intermittent milling

Parameter	Value
Spindle speed:	800 RPM
Cutting speed:	1.02 m/min
Axial depth of cut:	0.61 mm
Coolant:	Not used

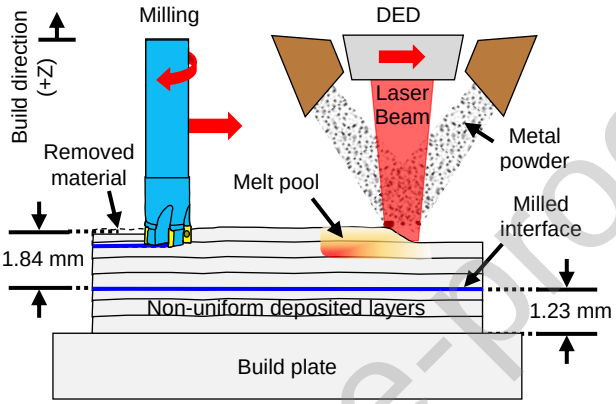

Fig. 4 Schematic of hybrid AM using DED and milling.

Two types of samples were manufactured to study interlayer milling during DED, *i.e.*, as-printed and hybrid samples. As-printed samples were manufactured using only DED. Hybrid samples were manufactured by repetition of steps: (1) depositing four layers using DED and (2) removing excess deposited material by *in situ* milling. Four layers meant approximately 1.84 mm tall material deposition before milling with a depth of cut of 0.61 mm (*i.e.*, approximately 1.3 layers). Deposition of four layers ensured that depositions were sufficiently tall in spite of surface waviness that affects the actual depth of cut. Deposition was paused for 40 seconds during interlayer milling that introduced a thermal dwell time during sample fabrication. This dwell time was replicated in as-printed samples to match thermal histories with hybrid samples. Thus, intermittent milling was the only point of difference between as-printed and hybrid samples in fabrication. A pause in heat input after printing every fourth layer allowed Ti-6Al-4V to cool before deposition of the next layer. Low net heat input to depositions was shown to reduce residual stress and distortion [26].

2.3 Microstructural Analysis

2.3.1 Optical and Scanning Electron Microscopy

Microstructure samples were designed to be printed to the same height of 30 mm with a theoretical layer thickness of 460 µm. This corresponded to 68 layers in the as-printed sample and 88 layers in the hybrid sample. The hybrid sample had more layers as interlayer milling removed 0.61 mm (*i.e.*, 1.3 layers) for every four layers deposited by DED. As a result, the hybrid samples were shorter than the as-printed samples. The concentration of machined interfaces in hybrid samples was 0.71 interfaces per millimeter of depth. The machining-induced interruption to printing was replicated in the as-printed sample by pausing for 40 seconds after every four layers. The resultant concentration of dwell interfaces in the as-printed samples was 0.51 interfaces per millimeter depth.

Samples were sectioned from the build plate and cut in half by wire-electrical discharge machining (wire-EDM) before microstructure evaluation. Approximately 2 mm of wire cut surface was removed using

320 grit polishing pads with water as coolant to minimize effects of wire-EDM. Surfaces were ground using incremental grit sizes of 400, 600, 800, and 1200. Polishing was performed using a nylon cloth and 6 µm diamond paste, followed by Lecloth® pads with 3 µm and 1 µm premium suspensions. All metallurgical supplies were purchased from Leco Corporation®. The polished surfaces of samples had mirror finish and were etched using Kroll's reagent (2 % HF + 6 % HNO_3 + 92 % H_2O). The polished and etched cross-section of the sample is shown along with dimensions in Fig. 5.

Optical and SEM images of etched surfaces were obtained using an optical microscope and FEI Helios NanoLab 660, respectively. Regions of samples that experienced similar numbers of heating and cooling cycles were selected for microscopy. The inspection areas were marked as regions 1, 2, and 3 on the samples to indicate bottom, middle, and top of the samples. Energy dispersive X-ray spectroscopy was performed on dwell and machined interfaces in region 2 of as-printed and hybrid samples.

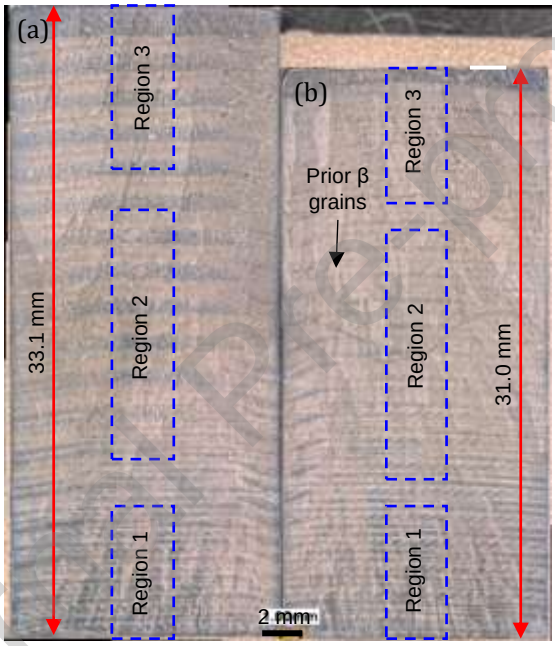

Fig. 5 (a) As-printed and (b) hybrid samples showing prior β-grain growth across multiple layers.

2.3.2 Ultrasonic Measurements

Ultrasound waves propagated through polycrystalline materials capture microstructural information as grain noise. The waves scatter at grain boundaries due to a mismatch of acoustic impedance [31]. Scattering of ultrasound opposite to the incidence direction due to microstructure is called backscatter and is used to characterize polycrystalline materials. Backscattering levels are indicative of the underlying grain morphology and elastic properties. The grain size relative to the wavelength controls the scattering amplitude. Consequently, larger grains cause higher backscatter [32, 33]. A diffuse field study that relies on backscatter due to microstructure at different depths within printed components enables spatial characterization of grain size. *In situ* characterization of mechanical behavior in addition to microstructure using ultrasound was previously demonstrated on hybrid AM manufactured Ti-6Al-4V using DED and interlayer milling [30]. Linear ultrasound signals propagated through hybrid samples was indicative of the elastic modulus. Ultrasound traversed slowly through β phase compared to α phase that signified lower elastic modulus in the β phase. Thus, a diffuse field study of hybrid AM samples enables characterization of grain size variation and elastic

modulus. Hence, ultrasound was used to quantify microstructure and elastic modulus at milled interfaces within printed Ti-6Al-4V.

Microstructure was assessed through ultrasonic measurements on un-sectioned samples from Fig. 5 using a transducer in a pulse-echo configuration. The transducer had 15 MHz nominal center frequency, 76.2 mm focal length, and estimated beam diameter of 600 μm [34]. At this frequency, the ultrasound scatters from the heterogeneities with higher scattering from the larger β phase. However, this study did not consider the influence of microtextured regions, which could lead to ultrasonic backscattering being misinterpreted as defects due to their highly localized presence within printed Ti-6Al-4V. Such effects from microtextured regions were not observed during backscattering measurements. The density measurements of the samples showed that they were all 98% dense. Thus, the contribution of backscatter from porosity is expected to be small and nearly the same for each sample.

The experimental setup was immersed under water and the material path was set at the center of the samples. Ultrasound waveforms were collected at steps of 0.5 mm along the X-Y plane. All samples had a square cross-section with 15 mm sides that corresponded to approximately 1024 waveforms collected per sample. Spatial variance of waveforms was attained by

$$\Phi_{exp}(t) = \frac{1}{N-1}\sum_{i=1}^{N} |Y_i(t) - Y_{mean}(t)|^2$$

where i^{th} waveform is a function of time increment, Δt, is $Y_i(t)$, mean waveform is $Y_{mean}(t)$, and N is total number of collected waveforms. The wave speed, c, was calculated as $c = 2d/\Delta t$, where d is sample height. The waves propagated from top, reflected at the bottom surface, and propagated back to the top. Consequently, waves travelled twice the sample height. Three replicates were analyzed for as-printed/hybrid samples.

2.4 Microhardness

Vickers microhardness measurements were performed using a 200 series Wilson Tukon Microindenter at a load of 300 gmf with 10 seconds hold time. The same polished samples from Fig. 5 were used for microhardness analysis. Indents were made on polished sample surfaces from the top to bottom along a straight line in -Z direction. ImageJ software was used to obtain dimensions of indents.

2.5 Residual Stress

Residual stress measurements were obtained by the hole-drilling method on 26 mm × 50 mm × 18 mm samples using MTS3000-Restan developed by SINT Technologies. Hole-drilling is a semi-destructive method of calculating residual stress based on measured strain. Strain measurements were taken using a 2 mm diameter end mill to drill through a strain gauge placed on the sample surfaces (Fig. 6). Hole-drilling was performed at a very high spindle speed of approx. 400,000 RPM, which led to a localized relaxation of stresses and strain released in the material. The software supplied by SINT Technologies uses the strain data to calculate the residual stresses in the material according to ASTM E837-13 standard.

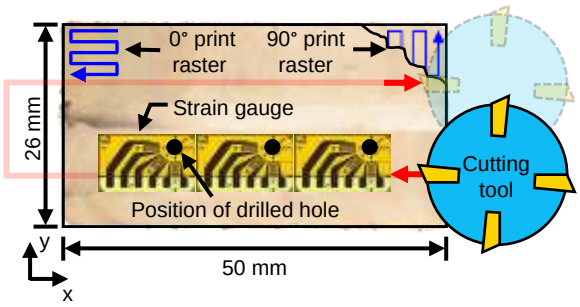

Fig. 6 Orientation of residual stress measurement with respect to printing and machining rasters.

The top surfaces of both as-printed and hybrid samples were milled to remove 2 mm before capturing residual stress by hole-drilling. Face milling conditions were 650 RPM, 0.083 mm/min, and 0.56 mm depth of cut. Milling was performed parallel to the long side of the samples. Three measurements were taken on each sample. The printed parts remained attached to their build plate until the end of hole-drilling experiments. Face milling on samples for surface preparation before residual stress measurement was along the same direction as inter-layer milling, *i.e.*, along X-axis.

2.6 Tensile Test

Static tensile tests were performed using Instron® universal testing machine (UTM) at a strain rate of 10^{-4}/s using dog-bone samples wire-EDM'ed from rectangular (25.4 mm × 6 mm × 2.5 mm) printed samples. Dog-bones were extracted from identical positions in samples and had gauge area dimensions (20 mm length and 6 mm width) as per ASTM-E8 [35]. The gauge thickness was 0.75 mm to conform with ASTM prescribed maximum thickness of 6 mm. The use of thin samples increased the number of samples that could be machined from the printed rectangular blocks of Ti-6Al-4V for tensile tests. As-printed, hybrid, and wrought samples were designed to have five replicates for the test. However, two hybrid samples failed during sample preparation and were omitted from the study.

Custom grips were designed for tensile tests to avoid any possibility of sample slipping during tensile test, as shown in Fig. 7. These grips held tensile samples at the curved sections above and below their gauge length to prevent slipping. A digital image correlator (DIC) was used to measure the strain in samples during tensile loading. The DIC equipment consisted of a high-speed camera (Basler Ace acA2440-75um) which captured images during tensile tests at 1 frame/second at 5 MP resolution. The camera was calibrated to correlate the distance between pixels to that of the distance between points on samples captured by camera.

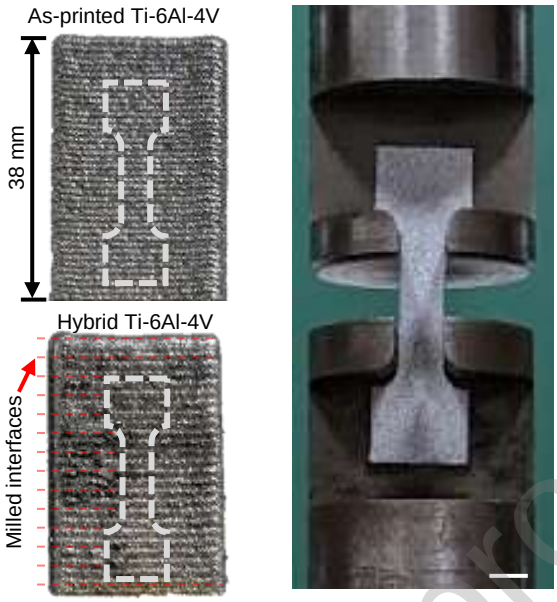

Fig. 7 (a) Tensile test specimens and (b) specimen held by grips during testing.

3. Results

3.1 Bulk Microstructure

Polished and etched samples revealed that macro-scale prior β grains grew opposite to the direction of heat flow, *i.e.*, along the build direction (*i.e.*, +Z-direction [10]) with minimal tilt due to raster pattern (Fig. 8). In hybrid samples, interlayer milling did not impose a barrier to epitaxial grain growth as prior β grains grew across machined interfaces. Laser induced heating for depositing subsequent layers after machining recrystallized surface microstructure and enabled growth of prior β grains at machined interfaces.

SEM images (Fig. 8) of the etched samples showed Widmanstätten α-laths within prior β grains (shown in Fig. 5), which is characteristic of DED Ti-6Al-4V [9]. Quantitative analysis by ImageJ software (Fig. 9) showed that the width of the laths progressively increased from the bottom to top in both as-printed and hybrid samples. Layers printed closer to the baseplate (*i.e.*, region 1) formed a small volume of deposition that dissipated heat quickly and resulted in fine α-laths. Heat retained within the print volume increased with addition of layers as the titanium has poor thermal conductivity [9]. Increased heat retention at higher temperatures formed coarser α-laths in the sample core (in region 2). The upper portion of the samples (*i.e.*, region 3) had coarser α-laths as the larger deposition volume enabled extended holding at high print temperatures. Energy dispersive X-ray spectroscopy performed across dwell and machined interfaces in region 2 of the two sample types found insignificant changes to chemical composition due to interlayer milling. Ultrasound characterization described in the next section attained continuous measurements of grain size along build height to identify microstructural alterations at milled interfaces within hybrid samples.

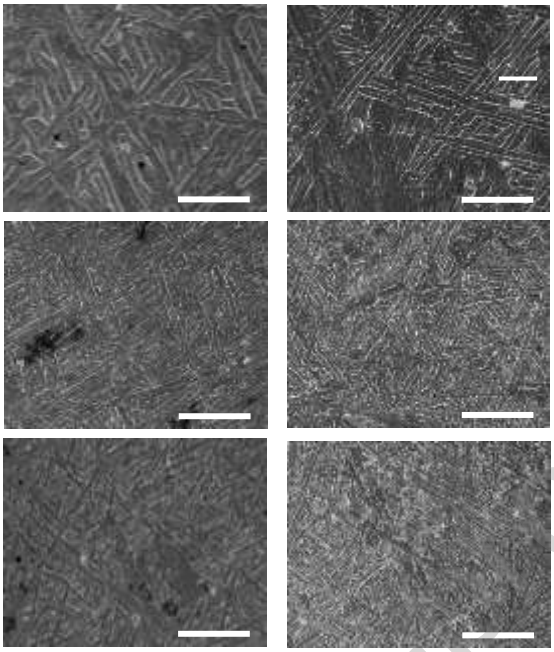

Fig. 8 SEM images of α-laths in (a) as-printed and (b) hybrid samples.

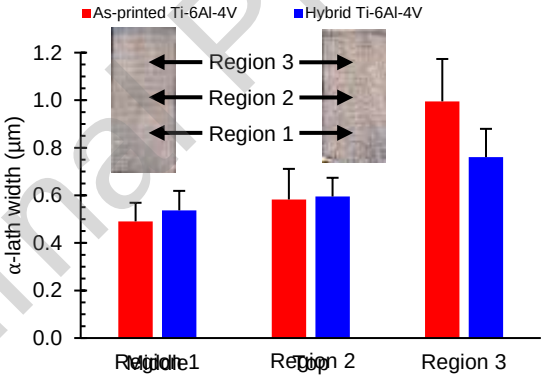

Fig. 9 α-lath grain widths at different heights for as-printed and hybrid AM Ti-6Al-4V.

3.2 Ultrasound Backscatter Measurements to Characterize Glocal Microstructure

3.2.1 Interface Spacing

Diffuse field ultrasound measurements through the top surface of samples provided a continuous map of milling- (in hybrid samples) and dwell- (in as-printed samples) influenced interfaces across the depth of printed Ti-6Al-4V. The spatial variance (Fig. 10) showed an overall reduction in the amplitude of ultrasound backscatter in hybrid samples that indicated the presence of larger number of scattering interfaces within the hybrid sample compared to as-printed samples [31-33]. The backscatter amplitude oscillated every 0.22 ± 0.03 μs in hybrid samples corresponding to the intervals of interlayer milling (Fig. 10). Oscillations in backscatter amplitude for as-printed samples were irregular and likely due to heterogeneity associated with DED. The distance between valleys of spatial variance plot for hybrid samples correspond to the distance

between milled interfaces. This valley-to-valley distance was ultrasonically determined to be 1.35 mm compared to the theoretical distance of 1.23 mm (measured as 4 × layer thickness − milling depth of cut). The diameter of the ultrasound beam was approximately 600 μm, which may explain the discrepancy between the actual and theoretical distance between milled interfaces. Thus, diffuse field measurements using ultrasound established the presence of regularly spaced machining-influenced microstructural interfaces within hybrid samples. This further supports the feasibility of using ultrasound for nondestructive evaluation in hybrid AM.

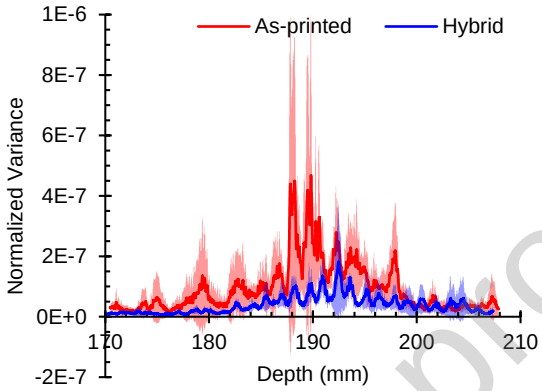

Fig. 10 Spatial variance of backscattered ultrasound projected from top surface of printed Ti-6Al-4V (curves represent avg. values and shaded regions depict max. and min. values).

3.2.2 Elastic Modulus

Ultrasound wave speed is proportional to the square root of elastic modulus of the media. The spatial variance in ultrasound measurements (Fig. 10) showed that backscatter intensity was high in both as-printed and hybrid samples at the focal depth of the ultrasound beam located approx. 190 mm below the top surface with corresponding wave propagation time of 30.5 μs. The wave speed measured through the three hybrid samples was 6.19 ± 0.00 mm/μs along the build direction compared to 6.20 ± 0.02 mm/μs in the as-printed samples. Thus, interlayer milling marginally lowered the average elastic modulus of printed samples.

3.3 Microhardness

3.3.1 Thermal Cancellation at Interfaces

The microhardness in printed samples was characterized to identify whether interlayer machining induced work-hardening or dynamic recrystallization was retained after being subjected to heat from the deposition of subsequent layers. Fig. 11 shows the variation in microhardness with depth in printed samples, wherein locations with low hardness corresponded to the machined and dwell interfaces (in as-printed and hybrid samples, respectively). The subsurface of these interfaces progressively hardened as the microstructure was replaced by fine α laths from previously deposited layers. The recurrence of high hardness in printed layers and low hardness near interfaces demonstrated that interlayer treatments were not thermally cancelled (*i.e.*, annealed) by the heat flux from deposition of subsequent layers. That is, microstructural alterations from interlayer milling were retained within the print volume.

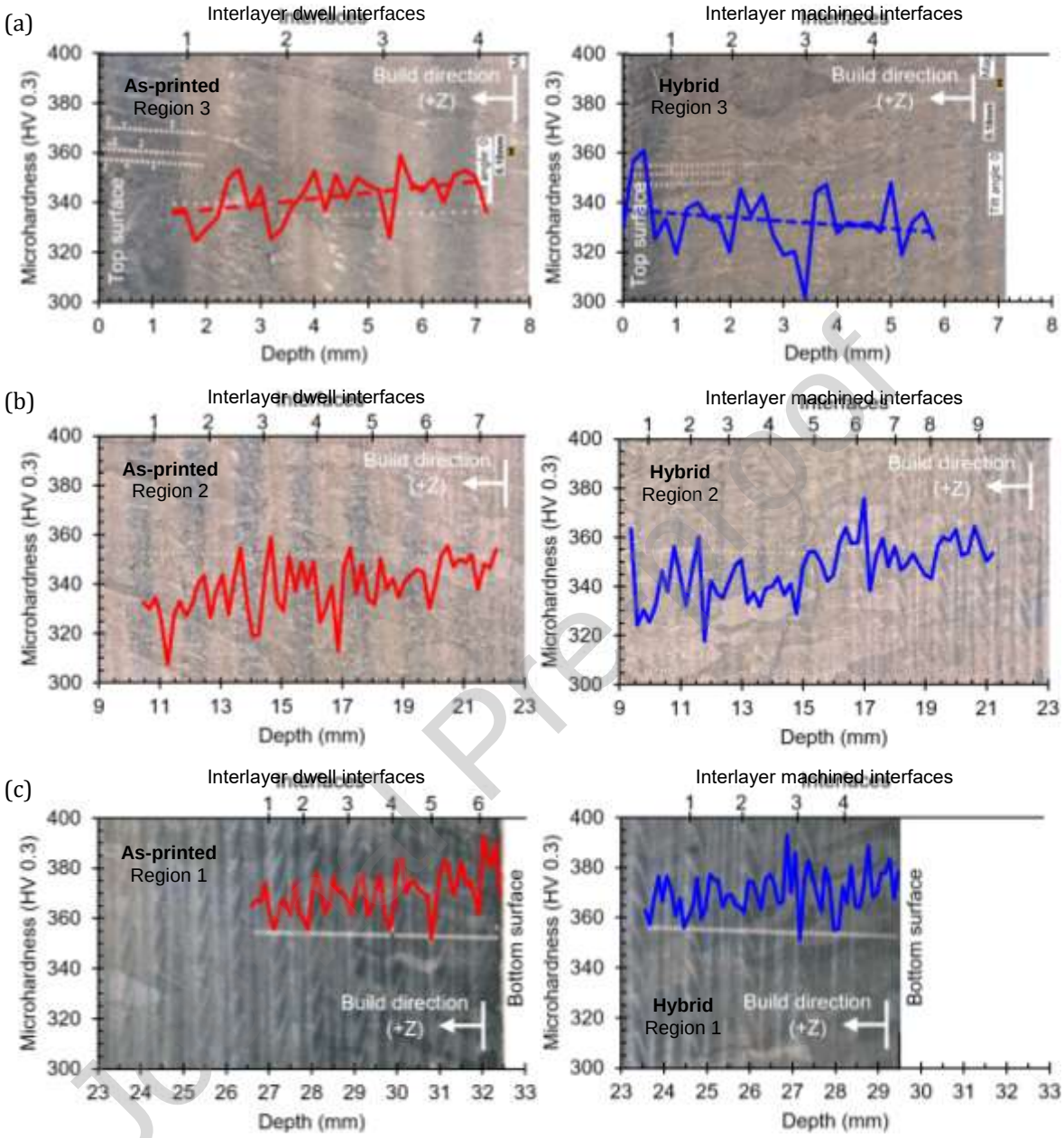

Fig. 11 Microhardness mapped across depth from (a) top, (b) middle, and (c) bottom of in as printed and hybrid Ti-6Al4V.

3.3.2 Dwell vs. Machined Interfaces

High resolution microhardness measurements on printed samples showed the final round of dry machining had hardened the top 200 µm hybrid sample compared to the as-printed sample (Fig. 12). This indicates that work-hardening dominated over dynamic recrystallization during interlayer milling. However, the hardness of interfaces in both sample types was lower than the hardness of the top surface. Hardness at these interfaces was further quantified to identify the extent of thermal cancellation. Characterization of interfacial differences in the two sample types would quantify how much thermal dwell induced grain coarsening contributed towards lowering the hardness of machined interfaces in hybrid samples. Fig. 13 shows that both dwell and

machined interfaces exhibited similar hardness, which indicates that work-hardening was insignificant compared to grain coarsening at machined interfaces. Any work hardening that occurred at the machined interfaces was likely recrystallized by the heat from DED of subsequent layers. Only thermal dwell induced coarse microstructure was retained at the interfaces.

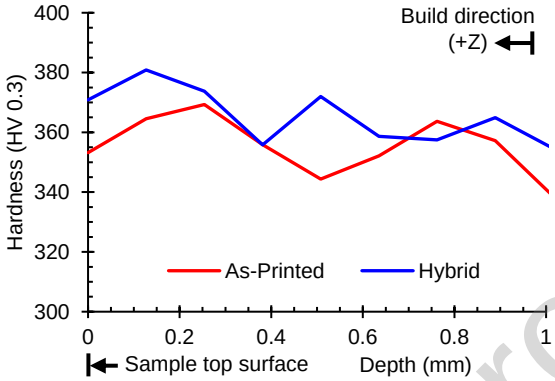

Fig. 12 High resolution microhardness measurements in the top 1mm of printed samples to indicate milling caused work hardening.

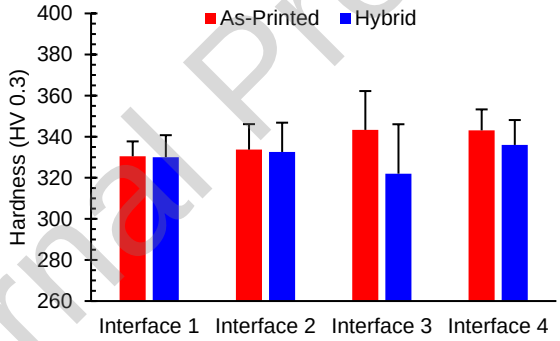

Fig. 13 Region 3 microhardness at dwell and machined interfaces identified in Fig. 11(a).

3.3.3 Interfaces vs. Interspatial Zones

Grain morphology at machined and dwell interfaces was different compared to regions between interfaces (referred to as interspatial zones). Dwell and machined interfaces had coarser grains compared to regions between interfaces. Slow cooling during thermal dwell cycles explains the local presence of coarse grains that lowered hardness at interfaces (Fig. 14(a, c)). These microstructural images confirm the observation made in Fig. 13 that work hardened microstructure was melted when subsequent layers were printed over the machined interfaces. Only coarse grains from thermal dwell during machining were retained in hybrid samples. Following a relationship analogous to Hall-Petch strengthening that relates yield stress to the inverse square root of α lath thickness [36, 37], the regions between interfaces with finer α laths showed higher hardness (Fig. 14(b, d)).

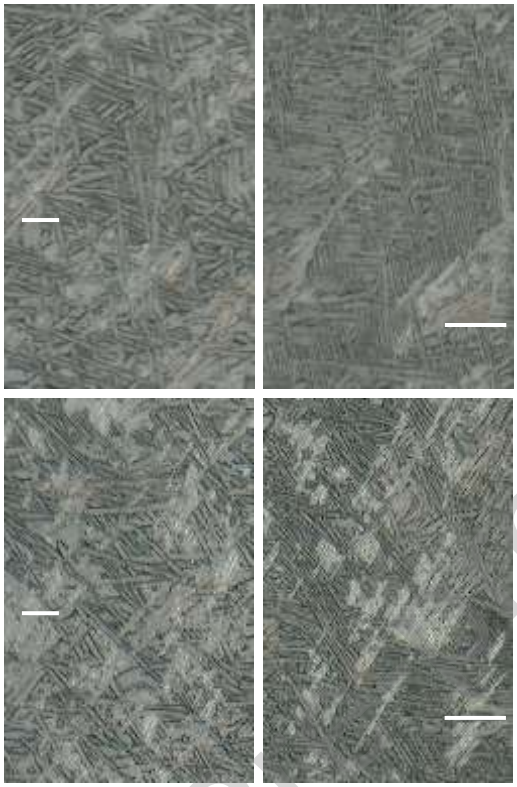

Fig. 14 Grain morphology at and between interfaces in the as-printed (a, b) and hybrid (c, d) samples.

Microhardness measured on printed samples was also used to verify the interface spacing identified by ultrasound backscatter from *Section 3.2*. Both microhardness and ultrasound backscatter experiments showed that machined interfaces in hybrid samples were tightly packed compared to dwell interfaces in as-printed samples (Fig. 15). Microhardness characterization substantiated this evidence by identifying tight and uniform interface spacing (1.35 mm) across the print volume in the hybrid sample. The interface spacing in as-printed samples was inconsistent across the build height and ranged from 1.83 mm in region 3 to 0.98 mm in Region 1.

3.3 Residual Stress

DED generates near-surface tensile stress that weakens and distorts parts, whereas milling on titanium induces compressive stress that improves surface integrity [38]. Hole-drilling revealed a 33% reduction in residual stress due to interlayer milling (Fig. 16). Beyond a depth of 0.2 mm that was affected because of surface preparation by face milling, tensile residual stress was consistently lower in hybrid samples. This result contrasts with machining on annealed Ti-6Al-4V, where compressive stress does not exceed 0.10 mm [25].

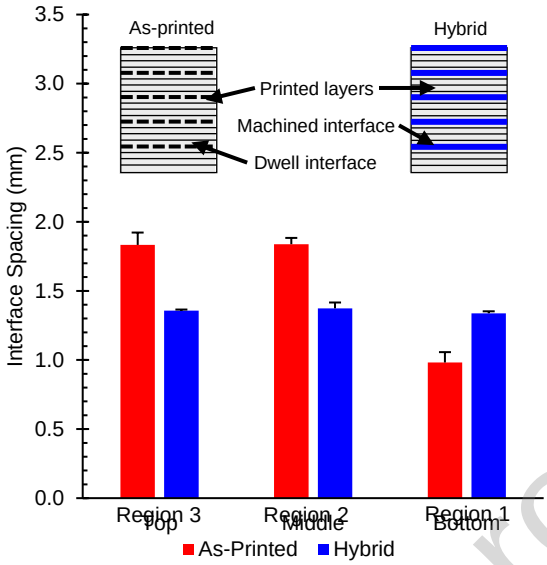

Fig. 15 Interface spacing in printed Ti-6Al-4V from microhardness characterization.

Residual stress along milling feed direction (σ_x) was larger than the stress in perpendicular direction (σ_y) for both sample types. Interlayer milling reduced σ_x by 32% and σ_y by 41% compared to as-printed samples. Further residual stress characterization was limited since hole drilling measurements are unreliable beyond 1 mm. Stress distribution across multiple milled interfaces were not mapped as the interval between milled interfaces was 1.35 mm, which is beyond the measurement limit of hole-drilling. Hybrid AM was anticipated to compound tensile stress from printing and compressive stress from machining to provide consistently low stress in hybrid samples across the build volume.

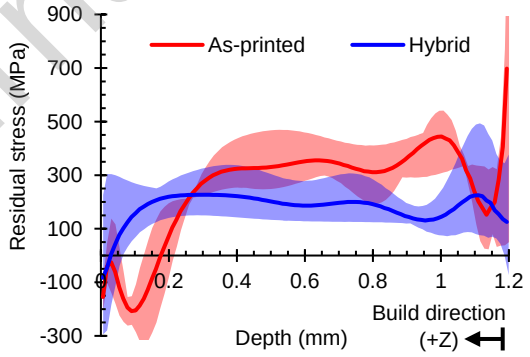

Fig. 16 Residual stress σ_x measured along the depth of as-printed and hybrid samples (curves represent avg. values and shaded regions depict max. and min. values).

3.4 Mechanical Properties

3.4.1 Tensile Behavior

Previous results characterized localized effects at machined and dwell interfaces in printed samples. This section describes the impact of these local interfaces on the bulk behavior of printed Ti-6Al-4V by tensile tests (Fig. 17). Tensile tests revealed that DED components had low ultimate strength along the build direction.

However, strain-to-failure for hybrid samples was 63% higher than as-printed and 8% higher than wrought. Interlayer machining improved ductility with negligible change to strength. Tensile tests showed a 5% reduction of average elastic modulus for hybrid samples compared to as-printed samples. The average elastic modulus characterized by tensile tests corroborated ultrasound wave speed analysis (6.19 ± 0.00 mm/μs and 6.20 ± 0.02 mm/μs, respectively). Table 3 provides quantitative analysis of tensile test.

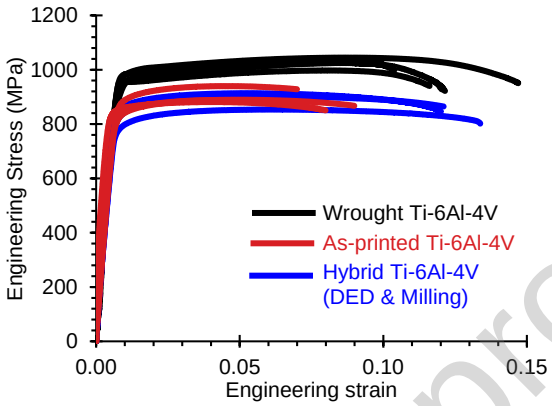

Fig. 17 Comparison of tensile behavior of as-printed and hybrid samples.

Table 3 Mechanical Properties

	Wrought	As-printed	Hybrid
UTS (MPa):	1025 ± 15	900 ± 21	889 ± 22
Yield Strength (MPa):	965 ± 14	844 ± 3	833 ± 30
Strain at Failure (%):	12 ± 2	8 ± 1	13 ± 1
Failure Strength (MPa):	966 ± 37	875 ± 28	837 ± 23
Elastic Modulus (GPa):	127 ± 16	129 ± 12	122 ± 8

3.4.2 Ductility

Printed samples with Widmanstätten α laths were less ductile compared to wrought annealed Ti-Al-4V. Interlayer placement of coarse grains in the hybrid samples recovered ductility that was lost from DED driven fine acicular α laths . The hybrid samples with higher concentration of machined interfaces (0.71/mm depth) were ductile compared as-printed samples with a dwell interface concentration of (0.51/mm depth). Higher content of coarse grains dispersed within the hybrid samples lowered resistance to dislocation mobility under external tensile stress, thereby contributing to the improved ductility. Coarse grains at milled interfaces were aided by the lower residual stress that delayed failure in hybrid samples compared to as-printed samples.

3.4.3 Fractography

Fig. 18 shows fracture patterns of Ti-6Al-4V dog-bone samples used for tensile tests. Three of five wrought samples fractured at approximately 45° indicating ductile behavior. As-printed and hybrid samples showed angular and flat failure paths indicating the presence ductile and brittle modes in the DED depositions. Scanning electron microscopy (SEM) was performed on the fractured surfaces (Fig. 19) to further investigate the modes of failure. All SEM images showed dimples from microvoid coalescence, which indicates a high toughness ductile fracture [39]. The micropores on as-printed and hybrid samples likely caused a stress concentration, leading to a reduced tensile strength. Although all samples exhibited microvoid coalescence, the size of the dimples on the printed samples varied significantly across the fractured surface compared to wrought samples. Fracture surfaces of wrought samples had larger and consistent sized dimples along with a few 100 μm flutes,

which suggest substantial local ductility [40]. Overall, microvoid coalescence on fractured surfaces indicates that all samples predominantly experienced ductile failure [39, 41]. Further analysis of the shear bands and fibrous zones observed on the fractured surfaces will be reported in a future publication.

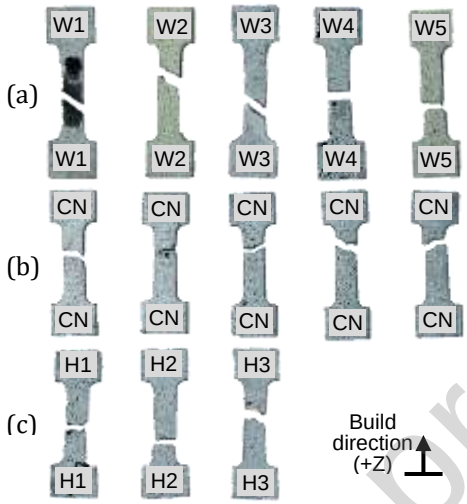

Fig. 18 Fracture patterns for (a) wrought, (b) as-printed, and (c) hybrid Ti-6Al-4V.

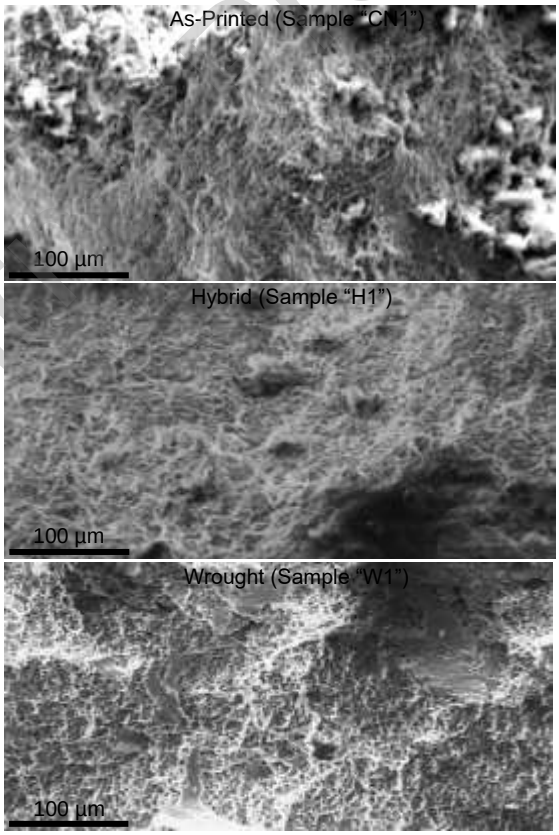

Fig. 19 Fractography of samples after tensile testing.

4. Discussion

4.1 Microstructure Formation from Hybrid Milling in DED

4.1.1 Work hardening vs. Dynamic Recrystallization:

The metallurgy of titanium from hot deformation is affected by competing phenomena of work hardening and dynamic recrystallization. Dynamic recrystallization is dominant in high stacking fault energy metals like α titanium during severe plastic (hot) deformation when the dislocation density is large [42]. Since dislocations accumulate at grain boundaries, strain-free grains from dynamic recrystallization nucleate at existing grain boundaries and alter local stress-strain behavior. The distribution of unstressed grains within a deformed microstructure enables dislocation motion that lowers hardness and strength while increasing plasticity. Work hardening is an alternative competing phenomenon in milled titanium that occurs at lower temperatures compared to dynamic recrystallization. Work hardening occurs when dislocation density within grains increases from plastically deforming processes like milling. Dislocations accumulated within grains restrict further dislocation motion that lowers the failure strain of the material but increases strength.

4.1.2 Thermal Cancellation of Work-hardened Interfaces:

Dry machining performed in this research resulted in work-hardening rather than dynamic recrystallization. Work-hardening was evidenced by the hard top surface of hybrid samples, where a final round of dry milling was performed. The top surfaces of the hybrid samples were harder (370 HV) than the un-milled top surfaces of the as-printed samples (360 HV) (Fig. 12). However, work hardening at prior milled interfaces within the hybrid samples was relieved by local heat from the DED during subsequent layer depositions over the interfaces. This thermal cancellation at machined interfaces was documented in Fig. 13 as the machined (in hybrid samples) and dwell (in as-printed samples) interfaces had statistically indifferent microhardness. Indifferent microhardness at machined and dwell interfaces identified thermal dwell time as the significant factor in microstructure formation of the printed titanium rather than work-hardening. Interruption to DED heat input during machining and dwell locally coarsened α-laths to produce low hardness at the interfaces compared to non-interface regions. The regions between interfaces (*i.e.*, non-interfaces) were harder due to the presence of fine α-laths (Fig. 14). Therefore, dynamic recrystallization and work hardening were not significant factors compared to thermal dwell time in influencing the local hardness and bulk ductility in hybrid AM titanium.

4.1.3 Microstructural Mechanisms in Hybrid AM

The proposed mechanism for microstructure formation in hybrid additive-subtractive manufacturing is depicted in Fig. 20. Fine α laths in DED titanium coarsened due to interrupted heat input during machining (in the hybrid sample) and dwell (in the as-printed sample). Machining over this coarse microstructure in hybrid samples accumulated dislocations from work-hardening, which locally improved tensile strength and reduced plasticity. When the work-hardened surfaces were subjected to heat from deposition of subsequent layers, the interfaces were partially recrystallized that annihilated dislocations. The coarse microstructure below the work-hardened regions were retained due to limited heat penetration as titanium has poor thermal conductivity. The extent of heat energy that penetrated machined interfaces in hybrid samples was analytically investigated using the equation for the Newton's law of cooling,

$$Q = k * \left(\frac{\pi D^2}{4}\right) * \frac{(T_{liquidus} - T_{recrystallization})}{L}$$

where, Q is the DED heat input (500 W), k is the thermal conductivity (20 W/mK) [15], D is the laser spot diameter (600μm), L is the depth that heat penetrates into printed titanium, $T_{liquidus}$ and $T_{recrystallization}$ are

the liquidus (1660 °C) [9] and recrystallization (850 °C) [16, 43] temperatures of Ti-6Al-4V. Newton's law of cooling showed that when a molten layer is deposited over machined and dwell interfaces, microstructural recrystallization does not exceed 5 µm below the meltpool depth. Since the meltpool depth in DED of Ti-6Al-4V is typically two layers tall, recrystallization was limited to a depth of approx. 455 µm below machined and dwell interfaces. In contrast, coarse grains from thermal dwell were observed 500 µm below interfaces (as seen in Fig. 14 (a, c)). Therefore, work-hardening induced grain refined regions (less than 15 µm deep) [25, 44] were recrystallized and only coarse grains from thermal dwell were retained. The coarse grains interfaces improved the bulk plasticity of hybrid samples more than the as-printed samples due to a higher concentration of milled interfaces (0.71/mm depth) compared to the dwell interfaces in the as-printed samples (0.51/mm depth) (Fig. 11). The results and analysis of this study validate the first and last stages of proposed mechanism for microstructure formation at machined and dwell interfaces in hybrid AM (Fig. 20). The dislocation formed in the intermediate stage from interlayer work-hardening was exhibited in prior publications [42, 45, 46].

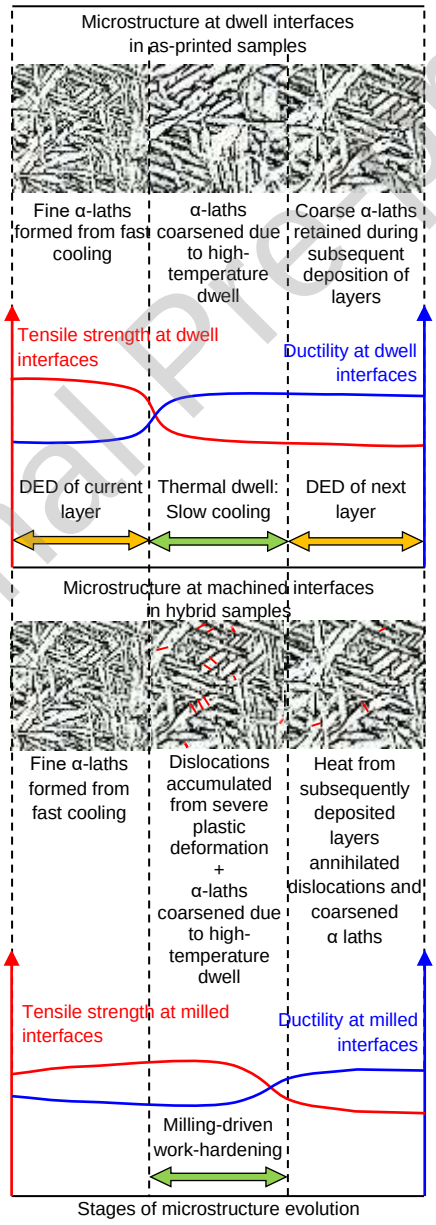

Fig. 20 Proposed mechanism for Ti-6Al-4V microstructure formation from interlayer milling (adapted from [42, 45, 46]).

4.2 Thermomechanical vs. Mechanical Interlayer Processing in Hybrid AM

Prior publications show that ductility imparted from interlayer processing is subjective to the intensity of treatments [24, 28, 47, 48]. Low intensity ultrasonic peening during powder bed fusion strain hardened 316 stainless steel, which increased strength but lowered ductility [24, 47]. In comparison, high intensity (500 % coverage) and high strain rate (> 10^5/s) deformation from laser peening introduced dynamic recrystallization that increased ductility [28, 48]. Dry milling complicates the balance between work hardening and thermal softening by introducing a heat flux from sliding friction near the cutting tool that lowers resistance to dynamic recrystallization. In this research, work hardening was dominant over dynamic recrystallization at machined interfaces, but the work-hardening was thermally cancelled by deposition of subsequent layers. Interruption to DED heat input during milling coarsened the microstructure of titanium and increased bulk plasticity of the hybrid samples. Therefore, the recurrent and inherent slow cooling of printed titanium during interlayer machining was important in dictating microstructure formation.

The results represented in this publication demonstrate how localized thermodynamics from dwell time during printing was the dominant mechanism for increased ductility of printed Ti6Al4V. Interlayer milling enabled the incorporation of a large concentration of coarse grain interfaces that improved bulk plasticity without any post-processing.

5. Summary and Conclusions

Hybrid AM using DED and face milling was investigated to determine the influence of interlayer cutting on material properties of Ti-6Al-4V. The overarching research objective was to understand how the cumulative exposure to high temperature severe shear plastic deformation affects bulk strength and ductility of Ti-6Al-4V through the physical phenomenon of grain refinement, residual stress relieving, work hardening, and dynamic recrystallization. The results showed that localized microstructural and residual stress alterations from interlayer milling affected bulk tensile behavior. The following are key observations:

1. *Tensile Behavior:* Dry milling during DED introduced a dwell time in printing that caused grain coarsening to increase failure strain of Ti-6Al-4V while maintaining strength.
2. *Fracture:* Printed and wrought samples exhibited microvoid coalescence on the fracture surface, indicating ductile failure of all samples. Wrought samples additionally exhibited 100 μm flutes which explained the high ductility.
3. *Residual Stress:* Interlayer milling during DED reduced tensile residual stress by 33%. Reduced stress coupled with interlayer dispersion of coarse grains improved ductility by 63% while maintaining ultimate strength (Approx. 900 MPa) compared to as-printed Ti-6Al-4V.
4. *Microstructure:* Prior β grains grew opposite to the direction of heat flow in printed Ti-6Al-4V and crossed milled surfaces. Grain refinement at interlayer interfaces from interlayer milling did not impede growth of prior β grains. Backscatter measurements by ultrasound identified coarse acicular α-lath interfaces corresponding to interlayer milled regions in hybrid Ti-6Al-4V.
5. *Microhardness:* Microhardness in both as-printed and hybrid Ti-6Al-4V increased with depth due to prevalence of acicular α laths. Interlayer dispersion of coarse α laths (from dwell in printing) near machined interfaces lowered hardness compared to non-interface regions in the hybrid sample. The microhardness at machined interfaces was comparable to dwell interfaces in the as-printed sample as heat input from DED relieved work-hardening in the hybrid sample.

In conclusion, the metallurgical effects of machining were retained within the microstructure of hybrid printed parts. The shear friction from dry milling generated plastic deformation through work-hardening that refined surface α-laths. The α-laths in the subsurface coarsened due to the inherent and recurrent dwell time to printing that was introduced by interlayer milling. Heat from subsequent deposition of layers on machined surfaces recrystallized the surface microstructure but retained subsurface coarse α-laths . The distribution of coarse and fine α laths at and between machined interfaces introduced a spatially graded grain size distribution. The selectively machined interfaces with coarse α-laths enabled higher dislocation motion that improved the bulk ductility.

This study contributed novel insights into the field of hybrid AM by identifying microstructural mechanisms in additive-subtractive manufacturing. The findings of this research also demonstrated that subtractive interlayer processing significantly changes material performance. For the successful integration of hybrid additive-subtractive manufacturing in industrial settings, the development of efficient computational tools is crucial, with a particular emphasis on accurately predicting the material state after fabrication. An important aspect for modeling material behavior is comprehending how spatial arrangement of machined interfaces influences the mechanical behavior of printed components. Specifically, the frequency of interlayer milling and the extent to which each machining cycle impacts part performance must be understood. Therefore, future work will focus on identifying the optimal placement of surface treated interfaces to tailor mechanical behavior of printed components.

Declaration of interests

☒ The authors declare that they have no known competing financial interests or personal relationships that could have appeared to influence the work reported in this paper.

Acknowledgments

The research was performed in part in the Nebraska Nanoscale Facility: NSF National Nanotechnology Coordinated Infrastructure under award no. ECCS: 1542182, and with support from the Nebraska Research Initiative through the Nano-Engineering Research Core Facility at the Univ. of Nebraska-Lincoln. Additive manufacturing was completed in the Nebraska Engineering Additive Technologies (NEAT) Lab. Partial financial support was provided by NSF CMMI: 1846478.

References

[1] Özel, T., Sima, M., Srivastava, A.K., Kaftanoglu, B., 2010. Investigations on the effects of multi-layered coated inserts in machining Ti–6Al–4V alloy with experiments and finite element simulations, CIRP Annals 59, p. 77-82.
[2] Flynn, J.M., Shokrani, A., Newman, S.T., Dhokia, V., 2016. Hybrid additive and subtractive machine tools – Research and industrial developments, International Journal of Machine Tools and Manufacture 101, p. 79-101.
[3] ASTM International, 2015. Standard Terminology for Additive Manufacturing.
[4] Wolff, S., Lee, T., Faierson, E., Ehmann, K., Cao, J., 2016. Anisotropic properties of directed energy deposition (DED)-processed Ti–6Al–4V, Journal of Manufacturing Processes 24, p. 397-405.
[5] Liu, Z., He, B., Lyu, T., Zou, Y., 2021. A review on additive manufacturing of titanium alloys for aerospace applications: directed energy deposition and beyond Ti-6Al-4V, JOM 73, p. 1804-1818.
[6] Sealy, M.P., Madireddy, G., Williams, R.E., Rao, P., Toursangsaraki, M., 2018. Hybrid processes in additive manufacturing, Journal of manufacturing science and engineering 140.

[7] Lu, J., Lu, H., Xu, X., Yao, J., Cai, J., Luo, K., 2020. High-performance integrated additive manufacturing with laser shock peening –induced microstructural evolution and improvement in mechanical properties of Ti6Al4V alloy components, International Journal of Machine Tools and Manufacture 148, p. 103475.
[8] Kalentics, N., de Seijas, Manuel Ortega Varela, Griffiths, S., Leinenbach, C., Logé, R.E., 2020. 3D laser shock peening – A new method for improving fatigue properties of selective laser melted parts, Additive Manufacturing 33, p. 101112.
[9] Liu, S., Shin, Y.C., 2019. Additive manufacturing of Ti6Al4V alloy: A review, Materials & Design 164, p. 107552.
[10] Saboori, A., Gallo, D., Biamino, S., Fino, P., Lombardi, M., 2017. An overview of additive manufacturing of titanium components by directed energy deposition: microstructure and mechanical properties, Applied Sciences 7, p. 883.
[11] Lia, F., Park, J.Z., Keist, J.S., Joshi, S., Martukanitz, R.P., 2018. Thermal and microstructural analysis of laser-based directed energy deposition for Ti-6Al-4V and Inconel 625 deposits, Materials Science and Engineering: A 717, p. 1-10.
[12] Mussatto, A., Groarke, R., Vijayaraghavan, R.K., Hughes, C., Obeidi, M.A., Doğu, M.N., Yalçin, M.A., McNally, P.J., Delaure, Y., Brabazon, D., 2022. Assessing dependency of part properties on the printing location in laser-powder bed fusion metal additive manufacturing, Materials Today Communications 30, p. 103209.
[13] Rey, P., Prieto, C., González, C., Tzimanis, K., Souflas, T., Stavropoulos, P., Rathore, J.S., Bergeaud, V., Vienne, C., Bredif, P., 2022. Data analysis to assess part quality in DED-LB/M based on in-situ process monitoring, Procedia CIRP 111, p. 345-350.
[14] Stavropoulos, P., Souflas, T., Bikas, H., 2021. Hybrid Manufacturing Processes: an experimental machinability investigation of DED produced parts, Procedia CIRP 101, p. 218-221.
[15] Parry, L., Ashcroft, I.A., Wildman, R.D., 2016. Understanding the effect of laser scan strategy on residual stress in selective laser melting through thermo-mechanical simulation, Additive Manufacturing 12, p. 1-15.
[16] Chuan, W., Liang, H., 2018. Hot deformation and dynamic recrystallization of a near-beta titanium alloy in the β single phase region, Vacuum 156, p. 384-401.
[17] Ginting, A., Nouari, M., 2009. Surface integrity of dry machined titanium alloys, International Journal of Machine Tools and Manufacture 49, p. 325-332.
[18] Sadeh, S., Mathews, R., Zhang, R., Sunny, S., Marais, D., Venter, A.M., Li, W., Malik, A., 2023. Interlayer machining effects on microstructure and residual stress in directed energy deposition of stainless steel 316L, Journal of Manufacturing Processes 94, p. 69-78.
[19] Ulutan, D., Ozel, T., 2011. Machining induced surface integrity in titanium and nickel alloys: A review, International Journal of Machine Tools and Manufacture 51, p. 250-280.
[20] Gwak, M., Kim, S., Lee, D.J., Seol, J.B., Sung, H., Nam, T., Kim, S., Kim, J.G., 2022. Post-annealing effect on the tensile deformation mechanism of a Ti–6Al–4V alloy manufactured via directed energy deposition, Materials Science and Engineering: A 836, p. 142729.
[21] Vastola, G., Zhang, G., Pei, Q.X., Zhang, Y.-., 2016. Controlling of residual stress in additive manufacturing of Ti6Al4V by finite element modeling, Additive Manufacturing 12, p. 231-239.
[22] Lu, X., Lin, X., Chiumenti, M., Cervera, M., Hu, Y., Ji, X., Ma, L., Yang, H., Huang, W., 2019. Residual stress and distortion of rectangular and S-shaped Ti-6Al-4V parts by Directed Energy Deposition: Modelling and experimental calibration, Additive Manufacturing 26, p. 166-179.
[23] Sealy, M.P., Hadidi, H., Kanger, C.J., Yan, X.L., Cui, B., McGeough, J.A., 2019. Glocal integrity in 420 stainless steel by asynchronous laser processing, CIRP Annals 68, p. 189-192.
[24] Wang, Y., Shi, J., 2019. Microstructure and properties of Inconel 718 fabricated by directed energy deposition with in-situ ultrasonic impact peening, Metallurgical and Materials Transactions B 50, p. 2815-2827.
[25] Zhao, W., Ren, F., Iqbal, A., Gong, L., He, N., Xu, Q., 2020. Effect of liquid nitrogen cooling on surface integrity in cryogenic milling of ti-6al-4 v titanium alloy, The International Journal of Advanced Manufacturing Technology 106, p. 1497-1508.
[26] Denlinger, E.R., Heigel, J.C., Michaleris, P., Palmer, T.A., 2015. Effect of inter-layer dwell time on distortion and residual stress in additive manufacturing of titanium and nickel alloys, Journal of Materials Processing Technology 215, p. 123-131.
[27] Kelly, S.M., 2004. Thermal and Microstructure Modeling of Metal Deposition Processes with Application to Ti-6Al-4V, Dissertation.

[28] Sealy, M.P., Hadidi, H., Sotelo, L.D., Li, W.L., Turner, J.A., McGeough, J.A., 2020. Compressive behavior of 420 stainless steel after asynchronous laser processing, CIRP Annals 69, p. 169-172.
[29] Webster, S., Lin, H., Carter III, F.M., Ehmann, K., Cao, J., 2021. Physical mechanisms in hybrid additive manufacturing: A process design framework, Journal of Materials Processing Technology 291, p. 117048.
[30] Sotelo, L.D., Karunakaran, R., Pratt, C.S., Sealy, M.P., Turner, J.A., 2021. Ultrasound in situ characterization of hybrid additively manufactured Ti6Al4V, The Journal of the Acoustical Society of America 150, p. 4452-4463.
[31] Song, Y., Kube, C.M., Turner, J.A., Li, X., 2017. Statistics associated with the scattering of ultrasound from microstructure, Ultrasonics 80, p. 58-61.
[32] Fu, Y., Hu, P., Turner, J.A., Song, Y., Li, X., 2019. Ultrasonic flaw detection for two-phase Ti-6Al-4V based on secondary scattering, NDT & E International 102, p. 199-206.
[33] Margetan, F.J., Gray, T.A., Thompson, R.B., 1991. A technique for quantitatively measuring microstructurally induced ultrasonic noise, Review of Progress in Quantitative Nondestructive Evaluation, p. 1721-1728.
[34] Ghoshal, G., Turner, J.A., Weaver, R.L., 2007. Wigner distribution of a transducer beam pattern within a multiple scattering formalism for heterogeneous solids, The Journal of the Acoustical Society of America 122, p. 2009-2021.
[35] ASTM International, 2016. ASTM E8/E8M-16ae1 standard test methods for tension testing of metallic materials, ASTM International.
[36] Jiang, Q., Li, S., Guo, S., Fu, M., Zhang, B., 2023. Comparative study on process-structure-property relationships of TiC/Ti6Al4V and Ti6Al4V by selective laser melting, International Journal of Mechanical Sciences 241, p. 107963.
[37] Xu, W., Brandt, M., Sun, S., Elambasseril, J., Liu, Q., Latham, K., Xia, K., Qian, M., 2015. Additive manufacturing of strong and ductile Ti–6Al–4V by selective laser melting via in situ martensite decomposition, Acta Materialia 85, p. 74-84.
[38] Köhler, J., Grove, T., Maiß, O., Denkena, B., 2012. Residual stresses in milled titanium parts, Procedia CIRP 2, p. 79-82.
[39] Ritchie, R.O., Liu, D., 2021. Chapter 6 - Micromechanics modeling of fracture, in *Introduction to Fracture Mechanics* R.O. Ritchie, D. Liu, Editors. Elsevier, p. 81-99.
[40] Pilchak, A.L., Williams, J.C., 2010. Crystallography of Fluted Fracture in Near-α Titanium Alloys, Metallurgical and materials transactions. A, Physical metallurgy and materials science 41, p. 22-25.
[41] ASM International, 1987. Titanium Alloys: Atlas of Fractographs, ASM Handbook 12, p. 441-455.
[42] Guo-Zheng, Q., 2013. Characterization for dynamic recrystallization kinetics based on stress-strain curves, Recent developments in the study of recrystallization, p. 61-64.
[43] Seo, S., Min, O., Yang, H., 2005. Constitutive equation for Ti–6Al–4V at high temperatures measured using the SHPB technique, International Journal of Impact Engineering 31, p. 735-754.
[44] Moritz, J., Seidel, A., Kopper, M., Bretschneider, J.ö, Gumpinger, J., Finaske, T., Riede, M., Schneeweiß, M., López, E., Brückner, F., Leyens, C., Rohr, T., Ghidini, T., 2020. Hybrid manufacturing of titanium Ti-6Al-4V combining laser metal deposition and cryogenic milling, The International Journal of Advanced Manufacturing Technology 107, p. 2995-3009.
[45] Lu, H., Deng, W., Luo, K., Chen, Y., Wang, J., Lu, J., 2023. Tailoring microstructure of additively manufactured Ti6Al4V titanium alloy using hybrid additive manufacturing technology, Additive Manufacturing 63, p. 103416.
[46] Du, H., Gong, Y., Xu, Y., Zeng, Q., Xiong, L., Li, Y., Nie, Y., Wang, J., Jin, X., 2022. Obtaining ultrastrong and ductile steel with hierarchical lamellar duplex phase microstructure by two-stage martensitic transformation mechanism, Metallurgical and Materials Transactions A 53A, p. 1613–1629.
[47] Gale, J., Achuhan, A., 2017. Application of ultrasonic peening during DMLS production of 316L stainless steel and its effect on material behavior, Rapid Prototyping Journal 23, p. 1185-1194.
[48] Kalentics, N., Boillat, E., Peyre, P., Gorny, C., Kenel, C., Leinenbach, C., Jhabvala, J., Logé, R.E., 2017. 3D laser shock peening – a new method for the 3D control of residual stresses in selective laser melting, Materials & Design 130, p. 350-356.